

Equilibrium Shapes and Their Stability for Liquid Films in Fast Flows

Likhit Ganedi,¹ Anand U. Oza,^{1,*} Michael Shelley,^{1,2} and Leif Ristroph^{1,†}

¹*Applied Math Lab, Courant Institute, New York University, New York 10012, USA*

²*Center for Computational Biology, Flatiron Institute, Simons Foundation, New York 10010, USA*



(Received 19 February 2018; published 31 August 2018)

We study how a suspended liquid film is deformed by an external flow en route to forming a bubble through experiments and a model. We identify a family of nonminimal but stable equilibrium shapes for flow speeds up to a critical value beyond which the film inflates unstably, and the model accounts for the observed nonlinear deformations and forces. A saddle-node or fold bifurcation in the solution diagram suggests that bubble formation at high speeds results from the loss of equilibrium and at low speeds from the loss of stability for overly inflated shapes.

DOI: 10.1103/PhysRevLett.121.094501

Soap films and bubbles are fascinating from many perspectives, not the least being the physics and mathematics of their shapes. Dipping a wire frame in soapy water yields a thin film that, due to surface tension, forms what can be idealized as a surface of minimal area [1–3]. Its shape is dictated by the Young-Laplace equation, which relates the pressure difference across an interface to its mean curvature [3,4]. The equality of pressures across an open film implies an equilibrium shape whose curvature is everywhere zero, and identifying such minimal surfaces consistent with a boundary has been a classic problem since first studied by Lagrange and Plateau [5–7]. Similarly, a spherical bubble is a closed surface that minimizes the area for a given volume. How a bubble is first formed involves the necking down and pinching off of a film. This event may be triggered, e.g., by separating two supports bridged by a liquid or film, as studied by Maxwell [8]. Recent work has focused on the collapse dynamics of fluid necks in the approach to pinch off [9–12] and on related topological transitions in films [13,14].

Our more common experience of making bubbles by blowing on a film is less studied and involves unique complexities. This event has been visualized in recent studies [15,16], and the competition of dynamic and Laplace pressures explains the critical flow speed needed to form bubbles [17]. Still unresolved is the flow-induced reshaping of a film, which even in equilibrium involves nonlinear deformations, incompressible flows into and around the film, and flow separation that forms a wake. These effects arise in other natural and industrial contexts, such as the ballooning and breakup of falling raindrops [18,19], water wave generation by wind [20], and the production of foams, emulsions, and sprays [21,22]. The mutual influence of interface shape and flow is a feature shared with many fluid-structure interactions [23,24], whose study often benefits from clean settings for a comparison of experiment and theory.

Here we consider the bubble-blowing problem in which a film suspended across a ring is deformed by the uniform flow of an exterior fluid. Recalling Plateau's use of immiscible liquid-liquid systems [5], we study oil films in flowing water, a system that offers advantages over soap film in air by mitigating the effect of gravity, eliminating evaporation, and permitting precise flow control, conditioning, and visualization. We also numerically construct 2D equilibria of a film distended by an inviscid but separated flow, with stable shapes qualitatively matching those seen in experiments and unstable shapes offering insight into how a bubble is blown.

Experiments.—We exploit a serendipitous discovery that some common oils can form large and long-lived films within water. By passing a wire loop through a layer of olive oil and into water below, one forms films that last for minutes before rupturing due to thinning by draining of the buoyant oil [25]. We employ olive oil as the interior fluid of density $\rho_i = 0.91 \text{ g/cm}^3$ immersed in the exterior fluid of

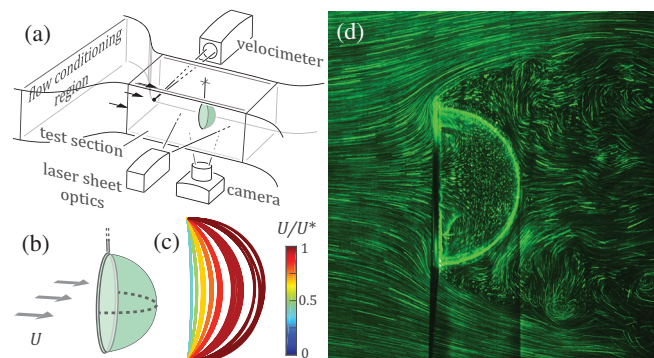


FIG. 1. Experiments. (a) Apparatus for studying the shape of, and flow around, an oil film in flowing water. (b) Schematic. (c) Measured profiles of stable shapes for speeds U up to U^* , at which the film ruptures. (d) Flow field near $U/U^* = 1$ for a ring of radius $R = 2 \text{ cm}$.

water, $\rho_e = 1.00 \text{ g/cm}^3$; their coefficient of surface tension is $\gamma = 17 \pm 1 \text{ dyn/cm}$, consistent with previous measurements [26]. The existence of stable films larger than the capillary length, $\sqrt{\gamma/(\rho_e - \rho_i)g} = 0.4 \text{ cm}$, suggests the presence of surfactants in the oil, perhaps residuals from processing [27]. To study the response to flow, we devise an apparatus that sits atop a water tunnel and allows for the repeatable formation of films on wire rings of radius $R = 1\text{--}3 \text{ cm}$. As shown in Figs. 1(a) and 1(b), the broadside of the ring faces the uniform oncoming flow of far-field speed $U = 1\text{--}10 \text{ cm/s}$ that can be varied and measured. The external flow is dominated by inertia at these high Reynolds numbers: $\text{Re} = \rho_e UR/\mu_e \sim 10^3$, where $\mu_e = 1 \text{ cP}$ is the viscosity of water. The flow-film interaction involves hydrodynamic and surface tension pressures, whose ratio is the Weber number $\text{We} \propto \rho_e U^2 R/\gamma \sim 1$, a scaled version of which will serve as the control parameter for this study.

When a film is placed within a flow of moderate speed, it is deformed from planar and settles to a dome- or parachutelike shape. The film then seems to be in stable equilibrium: It persists for minutes and recovers its shape after impulsive perturbations to the support or the flow speed. Such shapes exist up to a critical flow speed U^* , beyond which the film inflates unstably and ruptures (see Supplemental movie [28]). In Fig. 1(c), we show measured profiles for a ring of radius $R = 2.0 \text{ cm}$ for several values of U up to $U^* = 6.9 \text{ cm/s}$; 15 trials are shown at each of seven speeds selected from a set of 16 speeds. The film is nearly planar at low speeds and deforms into a hollow hemispherelike cavity as $U \rightarrow U^*$. However, the response is nonlinear in U , with the strongest changes occurring in the immediate lead-up to rupture. Additional analysis of the profile shapes is presented as Supplemental Material [28].

A visualization study reveals the character of the external flow. The photograph in Fig. 1(d) shows flow path lines [29] as revealed by microparticles illuminated by a planar laser sheet shone near the equator of a highly deformed film. Visual tracing of the incoming flow shows that only fluid very near the midline enters the cavity, where it abruptly slows down, as indicated by the short path lines. This internal flow slowly reverses course, following the inner contour of the film before abruptly speeding up and exiting near the support, where it separates from the surface to leave a large wake downstream.

Model.—To gain insight into the general features seen in experiments, we formulate a film-flow interaction model in a 2D setting, for which separated-flow models are well developed [30]. Flow separation is indeed a key ingredient, as purely inviscid and attached flow generates no pressure difference (akin to d’Alembert’s paradox [29]) and, thus, no film deformation. We consider a 2D exterior flow that is inviscid, incompressible, and irrotational and, hence, may be represented by a velocity potential in the complex plane. Separation is accounted for by Levi-Civita’s free-streamline

theory formulation [24,30,31], which uses conformal mapping [32] to solve for the potential as well as the path of the free or separation streamlines that shed tangentially from the pinning points and enclose a wake. Following previous studies [23,24,33,34], the wake flow is not explicitly modeled, but rather the wake pressure is assumed uniform, consistent with experimental measurements of the back pressure on bodies at high Re [35]. The film is viewed as a 1D curve pinned to two points separated by a (vertical) distance $2R$ and immersed within the exterior fluid of density $\rho_e = \rho$. The tension coefficient is γ , and the far-field flow is horizontal with speed U . The film is assumed static, and its equilibrium shape arises from the Young-Laplace law, which prescribes a local balance of differential hydrodynamic pressure and the surface tension pressure associated with curvature.

We highlight key steps of the model formulation, and supporting details are given in Supplemental Material [28]. Up-down symmetry permits focus on the half-space problem, and the film profile is given by the tangent angle $\theta(\sigma)$, where the parameter $\sigma \in [0, \pi/2]$ traverses the film. The local flow velocity \mathbf{u} along the film has a direction given by θ to ensure no penetration, and previous work [24] shows that the tangential speed $|\mathbf{u}|$ satisfies

$$|\mathbf{u}| = e^{\tau(\sigma)}, \quad \text{where } \tau = \mathcal{H}[\theta] \quad (1)$$

and \mathcal{H} is the Hilbert transform. Crucially, this indicates that the flow speed along the film can be computed from the shape alone. A second flow-shape relationship is furnished by combining the Young-Laplace and Bernoulli laws. The former relates the local pressure difference across an interface to its mean curvature, which for a zero-pressure wake and a film (two interfaces) yields $\Delta p = p = 2\gamma\kappa$. The latter relates the pressure and speed in the exterior flow: $p + \frac{1}{2}\rho|\mathbf{u}|^2 = \frac{1}{2}\rho U^2$. Combining to eliminate p yields the dimensionless curvature

$$\kappa R = R d\theta/ds = \eta[1 - (|\mathbf{u}|/U)^2], \quad \eta = \rho U^2 R/4\gamma, \quad (2)$$

where s is the arc length and η is akin to the Weber number. Recasting the above relationship in integral form yields

$$\theta(\sigma) = -\frac{\pi}{2} + K\eta \int_{\sigma}^{\pi/2} \sinh[\tau(\sigma')] \sin 2\sigma' d\sigma', \quad (3)$$

where the constant K is determined by the pinning condition at $\sigma = 0$. Solving this equation numerically by a Broyden method yields the equilibrium shape $\theta(\sigma)$ as a function of the dimensionless parameter η . The hydrodynamic force on the film is then given by an integral of pressure, and the entire 2D velocity and pressure fields can also be reconstructed.

We find that solutions exist only for $\eta \leq \eta^* \approx 1.0015$, which we associate with rupture. Selected profile shapes are shown in Fig. 2(a) at equally spaced $\eta/\eta^* \in [0, 1]$. In

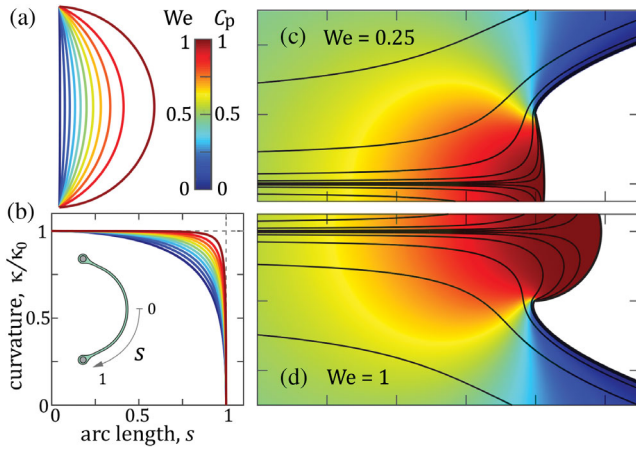


FIG. 2. Free-streamline theory model. (a) Equilibrium solutions at equally spaced $\eta = \rho U^2 R / 4\gamma$. (b) Profile curvature for the same solutions. (c),(d) Streamlines (black curves) and pressure coefficient C_p (color map) for $\eta/\eta^* = 0.25$ and 1. The wake (white) and far field have $C_p = 0$.

Fig. 2(b), we show the profile curvature κ scaled by its maximal value $\kappa_0 = \kappa(s=0) = \eta/R$ at the stagnation point and plotted versus the scaled arc length, where $s=0, 1$ denote the stagnation and separation points, respectively (see the inset). For each forcing, the curvature drops from its peak at stagnation to a value of zero at separation. For low η/η^* this drop is gradual, but as $\eta/\eta^* \rightarrow 1$ an ever greater portion of the interface takes on a value near κ_0 , and the shapes thus more closely resemble circular arcs.

In Figs. 2(c) and 2(d), selected streamlines (black curves) and the dimensionless pressure coefficient $C_p = 2p/\rho U^2 = 1 - (|u|/U)^2$ (color map) are compared for weak and strong forcing. The presence of the interface slows the oncoming flow, leading to higher pressures (red) in front, but the strongly deformed film of $\eta/\eta^* = 1$ has a

particularly large stagnated region inside the cavity where the pressure is more uniformly high. The streamlines show that a thin filament of incoming fluid spreads upon entering the cavity, dropping in speed (as required by continuity or mass conservation) and thus increasing in pressure (by Bernoulli's law). In essence, the stagnation point has spread into a broad region that encompasses much of the interface. These results indicate that the approach to rupture is marked by a tendency towards uniform pressure difference across the interface and, by the Young-Laplace law, uniform curvature.

Shape and force response.—The 3D film in the experiments differs from the 2D model in that both principal curvatures of the Young-Laplace law are nonzero: $\Delta p = 2\gamma(\kappa_1 + \kappa_2)$. Assuming axisymmetry, this leads to $\kappa_1 = \kappa_2 = \eta/2R$ at stagnation and $\kappa_1 = -\kappa_2$ at separation, and generally one expects different shape solutions in 3D and 2D [28]. A comparison of the model and experiment, however, reveals some common trends. The model indicates that 2D film rupture is associated with a critical η^* very near unity, and experiments on several ring sizes reveal a somewhat higher $\eta^* = \rho U^{*2} R / 4\gamma = 1.41 \pm 0.03$. In Fig. 3, we characterize the shape response to increasing η , normalized by the appropriate η^* for 2D and 3D. The plot in Fig. 3(a) shows the maximal deformation as measured (colored points) and computed (black curve), with both showing that the response is nonlinear even in $\eta \sim U^2$. A second parameter pertains to the extension of the film, as quantified by the surface area S in 3D and the total arc length L in 2D [Fig. 3(b)]. These quantities, when multiplied by γ , determine the surface energies stored in 3D and 2D interfaces, respectively [3,4]. The transition from flat (disk or line segment) at $\eta/\eta^* = 0$ to a hollow (hemispherical or semicircular) cavity at $\eta/\eta^* = 1$ yields the expected limits of $S/R^2 = \pi, 2\pi$ and $L/R = 2, \pi$. The response is again nonlinear, with most extension occurring in the immediate approach to $\eta/\eta^* = 1$.

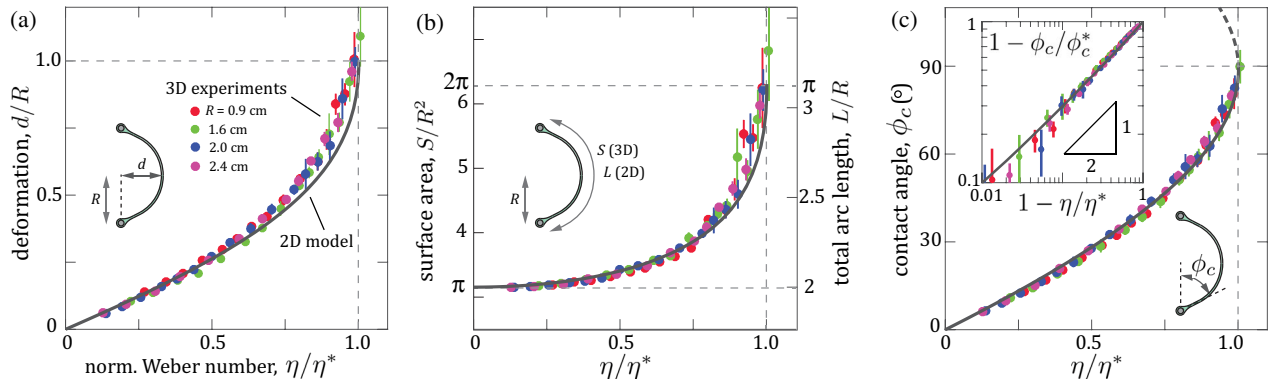


FIG. 3. Shape characterization. (a) Maximal deformation of the film versus normalized Weber number η/η^* in experiments (colored dots) and the model (black curve). (b) Film surface area S (experiments, left axis) and arc length L (model, right axis). (c) Contact angle ϕ_c of a film with support, with stable (solid curve) and unstable (dashed curve) branches from the model. The inset plot reveals a $1/2$ power typical of a fold bifurcation, with ϕ_c^* being the critical contact angle at rupture. Error bars for each experimental point represent standard deviations over 15 trials.

The contact angle ϕ_c of the film with the support, as defined in Fig. 3(c), also steeply increases en route to rupture at $\eta/\eta^* = 1$ and approaches $\phi_c^* \approx 90^\circ$ in experiments. The model reveals a second branch of solutions that can be accessed by decreasing η/η^* near this point. These interfaces have $\phi_c > 90^\circ$ and are overinflated into super-semicircular arcs. Superhemispherical shapes are never observed in experiments, suggesting that this upper branch represents unstable equilibria. This solution structure also indicates that overinflation is associated with a critical point in a saddle-node or fold bifurcation that occurs in the parameter η/η^* . To quantify this behavior, we consider a log-scaled plot of $1 - \phi_c/\phi_c^*$ versus $1 - \eta/\eta^*$ [Fig. 3(c), inset], which reveals a power-law approach to the critical point, here $(1 - \eta/\eta^*) \rightarrow 0$. The observed power near $1/2$ for both experiments and the model is typical of a saddle-node bifurcation [36]. Further analysis of the solutions can be found in Supplemental Material [28], including an argument supporting the stability of the lower branch and instability of the upper.

The contact angle also relates to the total hydrodynamic force exerted on the film. Integration of the pressure, which is proportional locally to the curvature, yields a formula for the force on a 3D axisymmetric film [28]: $F = 4\pi R\gamma \sin \phi_c$. The 2D analogue is a force per unit length of $F = 4\gamma \sin \phi_c$. Each case reveals a maximal force F^* (of $4\pi R\gamma$ in 3D and 4γ in 2D) that can be supported, which occurs for $\phi_c^* = 90^\circ$. From this perspective, overinflation occurs because the surface tension is unable to resist the imposed forces. The formula also provides a means for inferring the total force (here a drag) from the experimentally measured contact angle, and these data are shown as colored points in Fig. 4(a). The force extracted from the model (black curve) shows a similar trend, with no significant change in behavior as $\eta/\eta^* \rightarrow 1$, unlike the shape parameters in Fig. 3.

Close inspection of the force data reveals subtle nonlinearities, which correspond to deviations from the U^2 scaling expected for bodies of fixed shape in fast flows [29]. Indeed, the effect of shape is highlighted by the force coefficient $C_F = 2F/\rho_e U^2 A$, where $A = \pi R^2$ is the frontal area presented to the flow, which removes the expected scaling with the speed and size. This 3D coefficient and its 2D analogue of $F/\rho U^2 R$ for the model are shown in Fig. 4(b). Both increase with η/η^* , indicating an “anti-streamlining” behavior in which drag grows more strongly than U^2 as increasingly draggy parachutelike shapes are generated. The extremes of $\eta/\eta^* = 0, 1$ also correspond well with known values of $C_F \approx 1.2$ for a planar disk [37] (0.88 for a plate in the free-streamline theory [30]) and 1.4–1.5 for a hollow hemisphere [38]. A signature of the higher drag for greater η/η^* may also be seen in the wider wake in Fig. 2(d) as compared to Fig. 2(c).

The shape and force characterizations can be combined by assessing the force-displacement or stress-strain relationship, plotted as the dimensionless force F/F^* versus deformation d/R in Fig. 4(c). The film is Hookean for small forces, but thereafter the strain softens, yielding ever more in response to incrementally increased forcing.

Discussion.—This work reveals equilibrium shapes of flow-forced interfaces, which, unlike the area-minimizing surfaces formed by films and bubbles under hydrostatic conditions, have nonzero and nonuniform curvature. A model that solves for such shapes in 2D by locally balancing the Laplace and hydrodynamic pressures on a film in an inviscid but separated flow reproduces qualitative features and trends seen in 3D-axisymmetric experiments, including a nonlinear shape response leading up to rupture. The model also reveals a branch of unstable equilibria connected to the stable branch at the critical point of a fold bifurcation. This solution structure suggests that an unbounded distension of the film occurs at high speeds

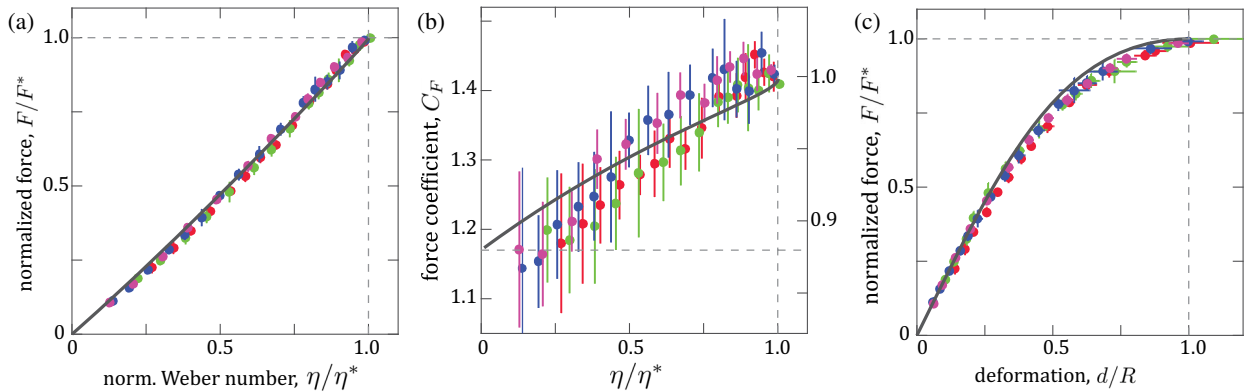


FIG. 4. Force characterization in experiments (dots) and the model (curve). (a) Total hydrodynamic force normalized by maximal values of $F^* = 4\pi R\gamma$, 4γ for 3D and 2D, respectively. (b) Force coefficients for 3D experiments (left axis) and the 2D model (right axis). The horizontal dashed line indicates drag coefficient values determined experimentally for a disk [37] and theoretically for a plate [30]. (c) A force-displacement plot shows strain softening in the approach to rupture. Experimental errors in $F/F^* = \sin \phi_c$ and $C_F = 2 \sin \phi_c / \eta$ are propagated from measured variations in ϕ_c .

beyond the critical point where no equilibria exist and also at lower speeds for which overly inflated shapes are unstable. These insights could be put to use in flow metrology, such as in designing film-based pressure probes or tensiometers, and in fluidic applications related to droplets, vesicles, and emulsions [39,40].

For our everyday experience with soap films, these findings offer a quasistatic picture of how an initially flat film is deformed by blowing at increasing speed before overinflating and forming a bubble. Surface tension opposes the imposed aerodynamic pressure across the film, which increasingly softens until the resisting force reaches its upper limit and the material fails. For the constant and uniform flow studied here, this failure involves overinflation, thinning, and rupture rather than making a water-filled oil bubble. In contrast, the birth of a soap bubble in air may result from the cessation of blowing once the film is overinflated. Indeed, an oil bubble can be generated underwater by an impulsive motion of the ring [28]. The form of the oncoming flow (i.e., uniform versus jetlike [17]) and the densities of two fluids (which impact the pinching dynamics) are additional factors that may decide between the ultimate fates of a ruptured film versus a blown bubble.

We thank S. Childress and J. Zhang for useful discussions. We acknowledge support from the grant NSF-CBET-1805506, from the postdoctoral fellowship NSF-DMS-1400934 to A. U. O., and from the Lilian and George Lyttle Chair.

*Present address: Department of Mathematical Sciences, New Jersey Institute of Technology, New Jersey, USA.

†ristroph@cims.nyu.edu

- [1] C. V. Boys, *Soap Bubbles, Their Colors and the Forces which Mold Them* (Dover, New York, 1959).
- [2] F. J. Almgren and J. E. Taylor, *Sci. Am.* **235**, 82 (1976).
- [3] C. Isenberg, *The Science of Soap Films and Soap Bubbles* (Dover, New York, 1992).
- [4] P.-G. De Gennes, F. Brochard-Wyart, and D. Quéré, *Capillarity and Wetting Phenomena: Drops, Bubbles, Pearls, Waves* (Springer, New York, 2013).
- [5] J. Plateau, *Mém. Acad. R. Sci., Lett. Beaux-Arts Belg.* **23**, 1 (1849).
- [6] J.-L. Lagrange, *Oeuvres de Lagrange* (Gauthier-Villars, Paris, 1870), Vol. 1.
- [7] R. Courant, *Am. Math. Mon.* **47**, 167 (1940).
- [8] J. C. Maxwell, in *The Scientific Letters and Papers of James Clerk Maxwell* (Cambridge University Press, Cambridge, England, 1990).
- [9] I. Cohen, M. P. Brenner, J. Eggers, and S. R. Nagel, *Phys. Rev. Lett.* **83**, 1147 (1999).
- [10] J. Eggers and E. Villermaux, *Rep. Prog. Phys.* **71**, 036601 (2008).
- [11] W. van Hoeve, S. Gekle, J. H. Snoeijer, M. Versluis, M. P. Brenner, and D. Lohse, *Phys. Fluids* **22**, 122003 (2010).
- [12] J. Bostwick and P. Steen, *Annu. Rev. Fluid Mech.* **47**, 539 (2015).
- [13] R. E. Goldstein, J. McTavish, H. K. Moffatt, and A. I. Pesci, *Proc. Natl. Acad. Sci. U.S.A.* **111**, 8339 (2014).
- [14] H. K. Moffatt, R. E. Goldstein, and A. I. Pesci, *Phys. Rev. Fluids* **1**, 060503 (2016).
- [15] D. Kim, S. J. Yi, H. D. Kim, and K. C. Kim, *J. Visualization* **17**, 337 (2014).
- [16] J. Davidson and S. Ryu, *J. Visualization* **20**, 53 (2017).
- [17] L. Salkin, A. Schmit, P. Panizza, and L. Courbin, *Phys. Rev. Lett.* **116**, 077801 (2016).
- [18] J. E. McDonald, *J. Meteorol.* **11**, 478 (1954).
- [19] A. Wierzbna, *Exp. Fluids* **9**, 59 (1990).
- [20] O. M. Phillips, *J. Fluid Mech.* **2**, 417 (1957).
- [21] D. L. Weaire and S. Hutzler, *The Physics of Foams* (Clarendon, Oxford, 1999).
- [22] P. Marmottant and E. Villermaux, *J. Fluid Mech.* **498**, 73 (2004).
- [23] S. Alben, M. Shelley, and J. Zhang, *Nature (London)* **420**, 479 (2002).
- [24] S. Alben, M. Shelley, and J. Zhang, *Phys. Fluids* **16**, 1694 (2004).
- [25] K. J. Mysels, *Soap Films: Studies of Their Thinning and a Bibliography* (Pergamon, New York, 1959).
- [26] P. Than, L. Preziosi, D. D. Joseph, and M. Arney, *J. Colloid Interface Sci.* **124**, 552 (1988).
- [27] D. Boskou, *Olive Oil: Chemistry and Technology* (American Oil Chemists' Society, Urbana, IL, 2015).
- [28] See Supplemental Material at <http://link.aps.org/supplemental/10.1103/PhysRevLett.121.094501> for text and two videos.
- [29] D. J. Tritton, *Physical Fluid Dynamics* (Clarendon, Oxford, 1988).
- [30] L. M. Milne-Thomson, *Theoretical Hydrodynamics* (Dover, New York, 1968).
- [31] A. R. Elcrat and L. N. Trefethen, *J. Comput. Appl. Math.* **14**, 251 (1986).
- [32] J. W. Brown and R. V. Churchill, *Complex Variables and Applications* (McGraw-Hill, New York, 2009).
- [33] L. Ristroph, M. N. Moore, S. Childress, M. J. Shelley, and J. Zhang, *Proc. Natl. Acad. Sci. USA* **109**, 19606 (2012).
- [34] M. N. Moore, L. Ristroph, S. Childress, J. Zhang, and M. J. Shelley, *Phys. Fluids* **25**, 116602 (2013).
- [35] R. Fail, R. Eyre, and J. Lawford, Aeronautical Research Council, Technical Report No. 3120, 1959.
- [36] S. H. Strogatz, *Nonlinear Dynamics and Chaos* (Westview, Boulder, CO, 2014).
- [37] F. W. Roos and W. W. Willmarth, *AIAA J.* **9**, 285 (1971).
- [38] H. G. Heinrich and E. L. Haak, Aeronautical Systems Division, Technical Report No. 61-587, 1961.
- [39] A. Utada, E. Lorenceau, D. Link, P. Kaplan, H. Stone, and D. Weitz, *Science* **308**, 537 (2005).
- [40] K. Funakoshi, H. Suzuki, and S. Takeuchi, *J. Am. Chem. Soc.* **129**, 12608 (2007).

Supplemental Material: Equilibrium shapes of a liquid film in a fast flow

Likhit Ganedi,¹ Anand U. Oza,² Michael Shelley,¹ and Leif Ristroph¹

¹*Applied Math Lab, Courant Institute, New York University, New York USA*

²*Department of Mathematical Sciences, New Jersey Institute of Technology, Newark, New Jersey, USA*

(Dated: 30 May 2018)

Analysis of experimental profiles. Here we provide additional analysis of the shapes from experiments and their curvature distributions. We focus on the critical condition just prior to rupture, for which the film is most distended and its curvature most pronounced. In Fig. 1, we display example sectional profiles (black dots) extracted from photographs for each of the four ring sizes tested. These are overlaid on perfect semicircular arcs (red) and shown at large scale and rotated so that shape details, slight asymmetries, and subtle deviations from circularity may be seen. Overall, these cross-sectional profiles appear very nearly circular over much of the shape, with significant deviations only near the pinning points. Deviations tend to be left-right asymmetries, which we associate with small-amplitude oscillations of the film.

To quantify the degree of uniformity in the shape, we examine in detail one such profile in Fig. 2, corresponding to the largest ring of radius $R = 2.4$ cm. In Fig. 2(a) we overlay extracted points (red) on the corresponding photograph so that the quality of tracking may be inspected. The striped pattern in the background is used to facilitate automatic extraction of the profile shape. To ease comparison, only every fourth extracted point is displayed. A zoomed-in view of the film near the ring support can be seen in Fig. 2(b), where all tracked points in this region are displayed.

Such high-resolution data is needed to accurately extract curvature, which involves first and second derivatives of the shape data. For a 3D surface, there are two principal curvatures: the in-plane or sectional component κ_1 and an out-of-plane component κ_2 . Considering each half of the measured shape as dictating a surface of revolution, we parametrize the surface using the streamwise coordinate x and an angle χ that corresponds to revolution about the x -axis. The measured sectional shape is a planar curve $y = f(x)$, and the 3D surface is then specified by: $x(\chi, x) = x$, $y(\chi, x) = f(x) \cos \chi$, $z(\chi, x) = f(x) \sin \chi$. The principal curvatures are given by

$$\kappa_1 = \frac{-f''}{(1 + f'^2)^{3/2}} \quad \text{and} \quad \kappa_2 = \frac{1}{f(1 + f'^2)^{1/2}} \quad (1)$$

where the signs have been selected so that concave shapes have positive curvature. Primes denote differentiation in x . The mean curvature is $H = (\kappa_1 + \kappa_2)/2$. These formulas permit the numerical computation of all relevant curvatures from the measured shape and its spatial derivatives.

In Fig. 2(c), we show the dimensionless in-plane curvature $\kappa_1 R$ as extracted for the left and right (blue and red) sides of the film separately. These are shown as functions of dimensionless arc length s/R along the profile starting at the most distended part near the middle and proceeding to the wire supports. The inset shows these curves at magnified scale, omitting the region near the wires. The in-plane curvature κ_1 can be seen to be nearly uniform and equal to $1/R$ over much of the film, with the variations primarily coming from differentiation of the profile shape data. Systematic deviations from uniformity of curvature are weak, consistent with the cross-sectional shape of Fig. 1 that closely resembles a semicircular arc. The abrupt drop in κ_1 near the wire, and its becoming negative, can be understood from inspection of Fig. 2(b). The curvature inverts in the region where the film thickens and connects to the wire ring via a meniscus. The positive spike in the κ_1 measurements at larger s/R reflects the high positive curvature of the wire cross-section.

Similar features are seen in the dimensionless mean curvature HR plotted in Fig. 2(d). The magnified inset again shows a highly uniform value of $H \approx 1/R$, implying a shape that closely resembles a hemispherical cap.

Comparison of 2D and 3D-axisymmetric films. Differences are expected for the 2D film considered in our model and the 3D film in the experiments. In Table I, we summarize some of the expected and observed differences. These arise because 2D films have only one non-zero principal curvature while 3D films have two such curvatures, as discussed above. Importantly, it is (twice) the mean curvature that appears in the Young-Laplace law: $\Delta p = 2 \times 2\gamma H = 2\gamma\kappa$ in 2D, while $\Delta p = 2 \times 2\gamma H = 2\gamma(\kappa_1 + \kappa_2)$ in 3D, where the prefactor of 2 comes from the film comprising 2 interfaces. Combining with Bernoulli's law and assuming a zero-pressure wake yields a local relationship between film curvature and tangential flow speed. In 2D, $\kappa R = \eta[1 - (|\mathbf{u}|/U)^2]$ where $\eta \equiv \rho U^2 R / 4\gamma$ is akin to the Weber number, while the analogous form in 3D is $(\kappa_1 + \kappa_2)R = \eta[1 - (|\mathbf{u}|/U)^2]$. Qualitatively, the effect is that a 2D film behaves as if more compliant than a 3D film, the latter bring stiffer since it resists external pressures by bending in both dimensions. Quantitatively, this leads to different profile shape solutions in 2D versus 3D as well as numerical differences (often involving a factor of 2) in some relevant quantities. For example, the stagnation pressure induces a dimensionless curvature of $\kappa R = \eta$ in 2D but $\kappa_1 R = \kappa_2 R = \eta/2$ in 3D. Hence, for the same value of η , the cross-section of a 3D film takes on an in-plane curvature at the stagnation point that is half that of a 2D

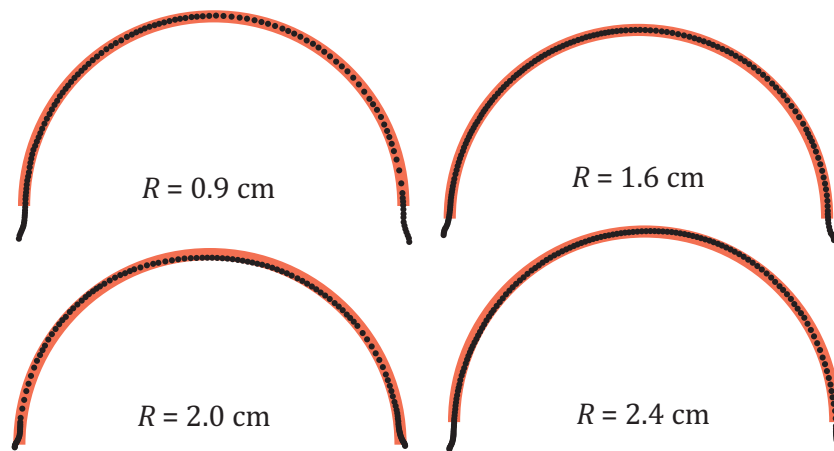


FIG. 1. Example tracked film profiles from experiments on four ring sizes, each at a flow speed just below the critical speed for rupture. Extracted points (black dots) are shown overlaid on semicircular arcs (red).

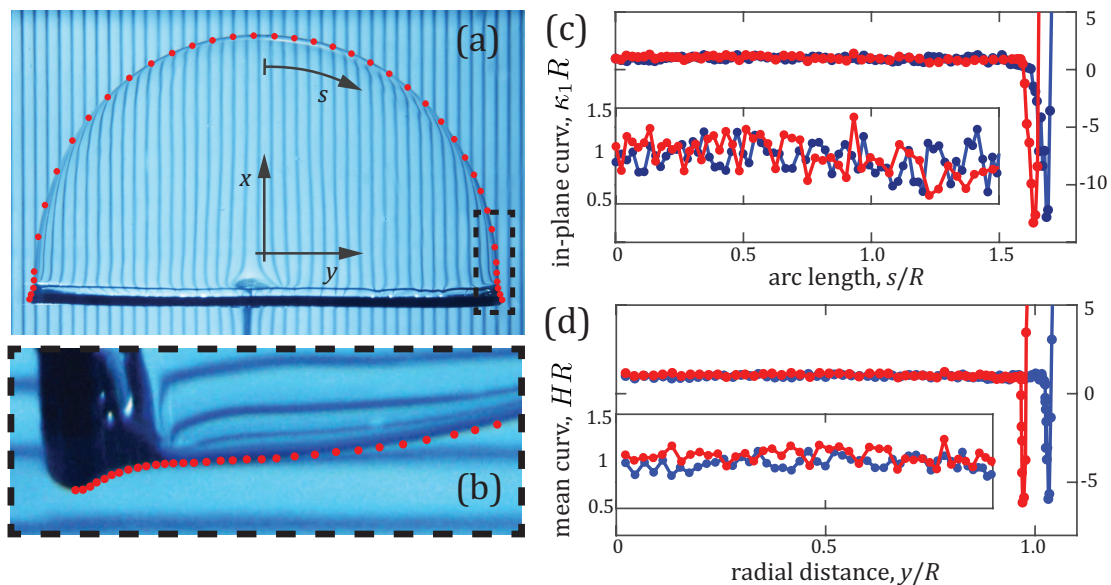


FIG. 2. Curvature analysis for a critical profile with $R = 2.4$ cm. (a) Photograph of film taken with striped background to facilitate interface tracking. Every fourth point from the shape extraction is shown. (b) Zoom-in on meniscus where the film meets the wire support. Every tracked point is shown. (c) Main: dimensionless in-plane curvature $\kappa_1 R$ plotted versus dimensionless arc length s/R along the left and right sides (blue and red) of the film. Inset: Zoom-in showing highly uniform curvature over much of the shape. (d) Similar plots of the dimensionless mean curvature HR .

film.

At the separation points, the pressure differential must be zero in both 2D and 3D. In 2D, this simply leads to $\kappa = 0$, as seen in Fig. 2(b) of the manuscript, and thus the film is flat where it joins the (vanishingly small) support. For 3D, we see that $H = 0$ and thus $\kappa_1 = -\kappa_2$. Interestingly, this means an ideal 3D-axisymmetric film is expected to be saddle-like where it meets its (vanishingly small) ring-shaped support. One expects a positive out-of-plane curvature $\kappa_2 > 0$ and thus $\kappa_1 < 0$ near the support. Thus a sectional view of the film should reveal a portion of inverted curvature whereas the majority of the profile has $\kappa_1 > 0$. To try to verify this in experiments, we have examined in detail the profile shape near

the wire, with an example zoomed-in image shown in Fig. 2(b). Indeed, one sees an inversion of curvature, but the interpretation is clouded by the presence of the wire and the associated meniscus or thickened portion of the film. A quantitative assessment can be made by measuring κ_1 in this region, as shown in Fig. 2(c), which reveals negative curvature in the near vicinity of the wire, $s/R \approx 1.6$. As the conditions are near critical and the shape nearly hemispherical, one expects $\kappa_2 R \approx 1$ and thus $\kappa_1 R \approx -1$. But in fact the curvatures are far more pronounced, dipping to values that are more than 10 times greater than expected. We thus conclude that the inverted curvature measured in experiments is strongly influenced by the meniscus.

	2D (or 3D-cylindrical)	3D-axisymmetric
Principal curvatures for $y = f(x)$	$\kappa_1 = \frac{-f''}{(1+f'^2)^{3/2}} \equiv \kappa$ and $\kappa_2 = 0$	$\kappa_1 = \frac{-f''}{(1+f'^2)^{3/2}}$ and $\kappa_2 = \frac{1}{f(1+f'^2)^{1/2}}$
Mean curvature	$H = \frac{1}{2}(\kappa + 0) = \frac{1}{2}\kappa$	$H = \frac{1}{2}(\kappa_1 + \kappa_2)$
Young-Laplace Law for film	$\Delta p = 2 \times 2\gamma H = 2\gamma\kappa$	$\Delta p = 2 \times 2\gamma H = 2\gamma(\kappa_1 + \kappa_2)$
Young-Laplace-Bernoulli relation	$\kappa R = \eta[1 - (\mathbf{u} /U)^2]$, $\eta \equiv \rho U^2 R/4\gamma$	$(\kappa_1 + \kappa_2)R = \eta[1 - (\mathbf{u} /U)^2]$
Stagnation point conditions	$ \mathbf{u} = 0$, $\Delta p = \frac{1}{2}\rho U^2$, $\kappa R = \eta$	$ \mathbf{u} = 0$, $\Delta p = \frac{1}{2}\rho U^2$, $\kappa_1 R = \kappa_2 R = \eta/2$
Separation point conditions	$\Delta p = 0$, $\kappa = 0$	$\Delta p = 0$, $\kappa_1 = -\kappa_2$
Force from film on support	$F = 2 \times 2 \times \gamma \sin \phi_c = 4\gamma \sin \phi_c$	$F = 2 \times 2\pi R \times \gamma \sin \phi_c = 4\pi R\gamma \sin \phi_c$
Force coefficient	$C_F = 2F/(\rho U^2 \cdot 2R) = \sin \phi_c/\eta$	$C_F = 2F/(\rho U^2 \cdot \pi R^2) = 2 \sin \phi_c/\eta$
Maximal force condition	$\phi_c = 90^\circ$, $F^* = 4\gamma$	$\phi_c = 90^\circ$, $F^* = 4\pi R\gamma$
Critical condition for rupture	$\eta^* = \rho U^{*2} R/4\gamma = 1/C_F^* \approx 1.0015$	$\eta^* = \rho U^{*2} R/4\gamma = 2/C_F^* = 1.41 \pm 0.03$

TABLE I. Comparison of relevant curvatures, pressure conditions, forces, and critical criteria for 2D (3D-cylindrical) and 3D-axisymmetric films. For the Young-Laplace equation and the force from the film on its support, a factor of 2 appears because the film comprises two interfaces. The force in the 2D case is given per unit length. The Young-Laplace-Bernoulli relation assumes a zero-pressure wake. The value of η^* is computed numerically in the 2D model and determined by measurements in the 3D experiments.

Dimensionality also introduces differences in the relevant forces for 2D and 3D films. The streamwise force that the film exerts on its support arises from its contact length and contact angle. In 2D, the force per unit length is $F = 2 \times 2 \times \gamma \sin \phi_c = 4\gamma \sin \phi_c$, where a factor of 2 comes from the film comprising 2 interfaces and another factor from the 2 support points. Each interface exerts a tension per unit length of γ , and $\sin \phi_c$ gives the streamwise component of the force given the contact angle ϕ_c . In 3D, the streamwise force is $F = 2 \times 2\pi R \times \gamma \sin \phi_c = 4\pi R\gamma \sin \phi_c$, where 2 interfaces make contact over a circumferential length of $2\pi R$. In both dimensions, this force assumes a maximal value for $\phi_c = 90^\circ$: $F^* = 4\gamma$ in 2D, and $F^* = 4\pi R\gamma$ in 3D. In Fig. 4(a) of the manuscript, we plot the normalized force F/F^* as a function of η . The formula $F/F^* = \sin \phi_c$, which holds in both 2D and 3D, allows us to infer the force from the experimental measurements of ϕ_c .

The force or drag coefficient is a non-dimensionalization that removes the expected scaling with fluid density, flow speed and film size. In 2D, $C_F = 2F/\rho U^2 \cdot 2R$, where $2R$ is the relevant projected area (per length) of the film. In 3D, $C_F = 2F/\rho U^2 \cdot \pi R^2$, where πR^2 is the projected area. This coefficient can be related to the contact angle through the $F(\phi_c)$ formulas given above, yielding $C_F = \sin \phi_c/\eta$ in 2D and $C_F = 2 \sin \phi_c/\eta$ in 3D. The latter allows us to extract C_F from the experimental measurements of ϕ_c , the results of which are displayed in Fig. 4(b) of the manuscript.

We associate film rupture with the condition of maximal force: $F/F^* = 1$ for $\phi_c = 90^\circ$ in both 2D and 3D. The critical flow speed needed to rupture the film can be found by using the appropriate force-speed ex-

pression involving C_F : $F = \frac{1}{2}\rho U^2 C_F \cdot 2R$ in 2D and $F = \frac{1}{2}\rho U^2 C_F \cdot \pi R^2$ in 3D. Setting $F = F^*$ leads to critical values of the flow speed U^* and the parameter $\eta^* = \rho U^{*2} R/4\gamma$, which is akin to the Weber number. In 2D, we see that $\eta^* = \rho U^{*2} R/4\gamma = 1/C_F^*$. In 3D, $\eta^* = 2/C_F^*$, the factor of 2 coming from dimensionality. Importantly, we thus observe that the value of η^* depends on the details of the critical shape through its drag coefficient C_F^* . As reported in the manuscript, numerical solutions of the 2D model show that $\eta^* \approx 1.0015$, while measurements of the critical speed for rings of different sizes in the 3D experiments yield $\eta^* = 1.41 \pm 0.03$.

(It may catch the reader's attention that, in both 2D and 3D, the values of η^* and C_F^* are very nearly equal. Both are quite close (but not exactly equal) to unity in 2D and quite close (within experimental error bars) to $\sqrt{2}$ in 3D. This seems to be pure coincidence. We know of no reason why these quantities ought to be similar beyond the fact that both are order-one parameters near the critical condition. A different definition of η , say without the factor of 4 in the denominator, would lead to less similar numerical values for η^* and C_F^* in both dimensions.)

Model formulation. Here we elaborate on the theoretical model described briefly in the main text. Our presentation closely follows the formulation and notation of Alben, Shelley and Zhang¹, which may serve as a companion exposition that provides additional derivations. As shown in Fig. 3(a), the film is modeled as a curve (solid black line) in the complex plane $z = x + iy$, and the external flow field (gray region) has complex velocity v . Each free or separation streamline (dashed curve) emanates tangentially from a pinning point (black and white dots), and its curve or path through space is to be com-

puted. Following the notation of Alben *et al.*, the flow may be described by a complex potential $w(z) = \varphi + i\psi$, where $dw/dz = \bar{v}$ and we non-dimensionalize by the speed U at infinity. This conformally maps streamlines to horizontal lines in the w -plane of Fig. 3(b). A second useful conformal map takes the form

$$w = (K/8)(\zeta + 1/\zeta)^2, \quad (2)$$

where K is an unknown constant to be determined. This ζ -plane is shown in Fig. 3(c), where the film is mapped to the unit semicircle $\zeta = e^{i\sigma}$, with $\sigma \in [0, \pi]$ being the (mapped) arc length. The free streamlines are mapped to the real axis $\zeta \in (-1, 1)$, the external flow is inside the semicircle, and the wake is outside. Non-dimensionalizing all spatial dimensions by the half-spacing R of the pinning points yields boundary conditions $\text{Im}(z) = \pm 1$ for the pinned ends. We assume the film to be up-down symmetric, and without loss of generality fix the stagnation point at the origin $z = 0$. We thus restrict our attention to $\sigma \in [0, \pi/2]$, which corresponds to the bottom half of the film.

It has been shown by Alben *et al.*¹ that

$$\frac{dz}{d\zeta} = \frac{K}{4} e^{i\Omega} \left(\zeta - \frac{1}{\zeta^3} \right), \quad \Omega = i \log(dw/dz), \quad (3)$$

from which it was derived that

$$\frac{dz}{d\sigma} = -\frac{K}{2} e^{i\theta} e^{-\tau} \sin 2\sigma \quad \text{and} \quad \frac{ds}{d\sigma} = \frac{K}{2} e^{-\tau} \sin 2\sigma. \quad (4)$$

Here, s is the physical arc length of the film, and $\theta(\sigma) + i\tau(\sigma)$ is the restriction of Ω to the film $\zeta = e^{i\sigma}$. The flow velocity along the film has direction θ identical to the film tangent angle (measured from the x -axis) and speed $|v| = e^\tau$. Since the film curvature κ can be written as $\kappa = (d\theta/d\sigma)/(ds/d\sigma)$, and since $\kappa = \eta(1 - e^{2\tau})$ follows from Eq. (2) in the main text, we obtain

$$\frac{d\theta}{d\sigma} = -K\eta \sinh[\tau(\sigma)] \sin 2\sigma. \quad (5)$$

Equation (3) in the main text is obtained by integrating this equation with the boundary condition $\theta(\pi/2) = -\pi/2$, which follows from up-down symmetry. Integrating Eq. (4) with the boundary condition $z(\pi/2) = 0$, and imposing that the film be pinned to the ring, $\text{Im}[z(0)] = -1$, we obtain an equation for the constant K :

$$\frac{1}{K} = -\frac{1}{2} \int_0^{\pi/2} \sin[\theta(\sigma')] e^{-\tau(\sigma')} \sin 2\sigma' d\sigma'. \quad (6)$$

Towards numerically solving Eq. (6) along with Eqs. (1) and (3) in the main text, we write $\theta(\sigma) = \theta_0(\sigma) + \tilde{\theta}(\sigma)$ and $\tau(\sigma) = \tau_0(\sigma) + \tilde{\tau}(\sigma)$, where

$$\theta_0(\sigma) = -\pi/2, \quad \tau_0 = \ln \left(\frac{\sin((\pi/2 - \sigma)/2)}{\sin((\pi/2 + \sigma)/2)} \right) \quad (7)$$

corresponds to the free streamline flow around a flat plate¹. That is, we explicitly remove the discontinuity in

θ due to the stagnation point at the middle of the film, thus making the problem numerically tractable. Substituting these expressions into Eq. (3) of the main text, we obtain the modified integral equation

$$\tilde{\theta}(\sigma) = -2K\eta \int_\sigma^{\pi/2} (\cosh[\tilde{\tau}(\sigma')] \sin^2 \sigma' - \sinh[\tilde{\tau}(\sigma')] \sin \sigma') d\sigma'. \quad (8)$$

Integrating Eq. (3) yields

$$z(\sigma) = -iK \int_\sigma^{\pi/2} (\sin \sigma' + \sin^2 \sigma') e^{i\tilde{\theta}(\sigma')} e^{-\tilde{\tau}(\sigma')} d\sigma', \quad (9)$$

and we obtain the modified form of Eq. (6) by imposing the boundary condition $\text{Im}[z(0)] = -1$:

$$\frac{1}{K} = \int_0^{\pi/2} (\sin \sigma' + \sin^2 \sigma') \cos[\tilde{\theta}(\sigma')] e^{-\tilde{\tau}(\sigma')} d\sigma'. \quad (10)$$

We solve Eqs. (8) and (10) numerically using a Broyden method, discretizing $\tilde{\theta}$ using 4096 equally-spaced points in the interval $\sigma \in [0, \pi/2]$. The Hilbert transform function in MATLAB is used to compute $\tilde{\tau} = \mathcal{H}[\tilde{\theta}]$, and all integrals are computed using the trapezoidal rule.

Drag computation. Given the solution $\theta(\sigma)$, we may now determine the total hydrodynamic force or drag on the film. The force per unit length \mathbf{F} on the film is given by integrating the pressure $p = 2\gamma\kappa = 2\gamma(d\theta/ds)$ multiplied by the unit outward normal \mathbf{n} :

$$\mathbf{F} = \int p \mathbf{n} ds = 2\gamma \left[\int_{-\theta_c}^{-\pi/2} (-\sin \theta, \cos \theta) d\theta + \int_{\pi/2}^{\theta_c} (\sin \theta, -\cos \theta) d\theta \right] = -4\gamma \cos \theta_c \hat{\mathbf{x}} = 4\gamma \sin \phi_c \hat{\mathbf{x}}, \quad (11)$$

where $\theta_c = \theta(\pi) \geq \pi/2$ is the film angle relative to the horizontal at the pinning point $\sigma = \pi$. We have used the film symmetry about the x -axis, and the final equality in Eq. (11) simply relates the force to the contact angle $\phi_c = \theta_c - \pi/2$ used in the main text. As is the convention in studies of droplets on surfaces, this contact angle is defined as the interior angle of the interface at the pinning point, e.g. $\phi_c = 0$ for a flat film and $\phi_c = 90^\circ$ for a semi-circle.

Film shape and flow streamlines. From the solution $\theta(\sigma)$ we may extract the film shape by evaluating Eq. (9) for $\sigma \in [0, \pi/2]$. To find the streamlines, we first extend Ω to the entire unit disk $|\zeta| \leq 1$. Following Alben *et al.*¹, we expand $\theta(\sigma)$ and $\Omega(\zeta)$ as

$$\theta(\sigma) = \sum_{k=0}^{\infty} a_k \cos k\sigma \quad \text{and} \quad \Omega(\zeta) = \sum_{k=0}^{\infty} a_k \zeta^k. \quad (12)$$

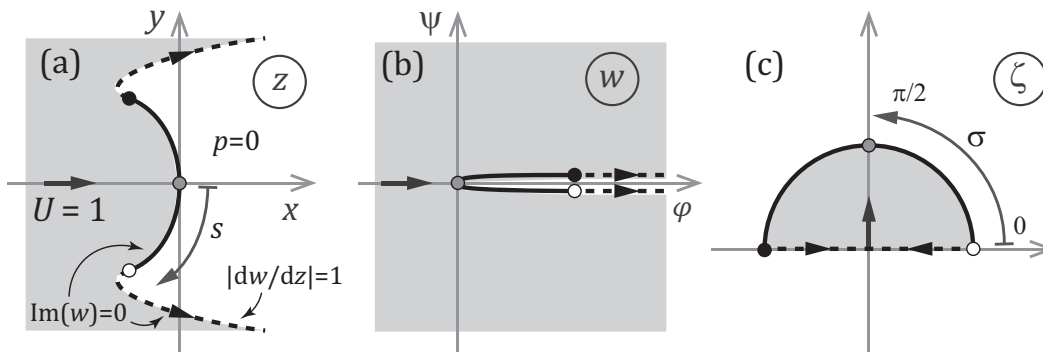


FIG. 3. Problem set-up and relevant domains. (a) Physical plane z , where the film (solid black curve) is pinned to two points (white and black dots) and immersed in the flow of an exterior fluid (gray). Separation streamlines (dashed curves) emanate from the pinning points and enclose a stagnant wake (white). (b) The w -plane maps streamlines (ψ constant) to horizontal lines. (c) The ζ -plane maps the film to the upper semicircle, with the flow inside and the wake outside.

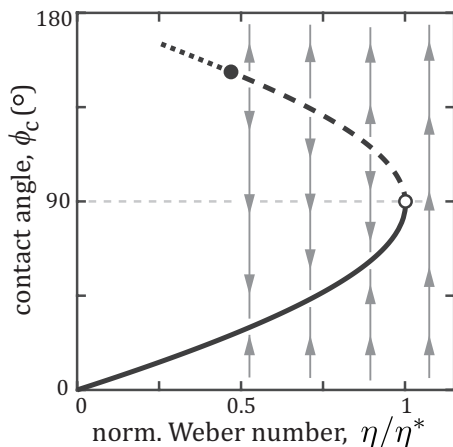


FIG. 4. Full solution map of equilibrium contact angles as a function of the normalized Weber number η/η^* . A lower branch of solutions (solid curve) may represent stable equilibria, while the upper branch (dashed) may be unstable, as indicated by the arrows. The dotted portion corresponds to unphysical solutions for which the streamlines intersect the film.

Note that $a_k = 0$ for k even, since up-down symmetry implies that $\theta(\pi/2 + \sigma) = -\theta(\pi/2 - \sigma)$ for $\sigma \in [0, \pi/2]$. Integrating Eq. (3), we obtain

$$z(\zeta) = \frac{K}{4} \int_1^\zeta e^{i\Omega(\zeta')} \left(\zeta' - \frac{1}{\zeta'^3} \right) d\zeta' + z|_{\zeta=1}, \quad (13)$$

where $z|_{\zeta=1}$ is obtained by evaluating Eq. (9) at $\sigma = 0$. The free streamline (corresponding to $\text{Im}[w] = 0$) is obtained by integrating Eq. (13) for $\zeta \in [-1, 1]$.

The remaining streamlines are computed by using Eq. (2) to construct the velocity potential $w(z)$ in the physical plane. Specifically, we discretize the first quadrant of the unit disk $|\zeta| \leq 1$ using $\zeta = re^{it}$ with equally spaced $r \in [0, 1]$ and $t \in [0, \pi/2]$. For a given point $\zeta = r_0 e^{it_0}$, Eq. (13) is evaluated numerically by first integrating along the real axis from $\zeta' = 1$ to $\zeta' = r_0$, and then along the arc $\zeta' = r_0 e^{it}$ for $t \in [0, t_0]$. We use MATLAB to numerically compute the level curves of $\text{Im}[w(z)]$,

which correspond to the flow streamlines.

Additional model results and their interpretation. Here we briefly describe additional model results pertaining to the upper branch of shape solutions. The full solution map is shown in Fig. 4. The contact angles of all equilibrium shape solutions are shown for varying normalized Weber numbers η/η^* , with $\eta^* \approx 1.0015$ representing the maximal value for which solutions are found. The lower branch of solutions (solid curve) corresponds well with the experimental data (see Fig. 3(c) in the main text), suggesting that they represent stable equilibria. The upper branch (dashed) may represent unstable equilibria, as argued in more detail below.

To better understand the two solution branches, we compare in Fig. 5(a) the two shape solutions corresponding to $\eta/\eta^* = 0.8$. The lower branch shape (blue) resembles a sub-semicircular arc, and the upper branch (red) resembles a super-semicircular arc. The two solutions very nearly complete a circle. That these solutions indeed have almost uniform curvature over the film and approximately the same value for this curvature is confirmed by the plots of Fig. 5(b). The curvature deviates from its stagnation value only in a small region near the support, where it must be zero. A comparison of the flow streamlines, speed, and pressure can be found in Fig. 5(c) and (d). Here the uniform curvature may be associated with the uniformly high pressure on the insides of these cavities.

Returning to the upper branch of Fig. 4, we note that following this branch backwards (decreasing η/η^*) yields more distended or inflated film shapes. Near $\eta/\eta^* \approx 0.5$ (black dot), we find that the shape becomes so distended that the free streamlines intersect the film itself. As η/η^* is decreased further (dotted curve), this feature persists and thus all solutions along this segment involve crossing streamlines. We interpret such solutions as being unphysical. This feature has been observed in previous studies of free streamline theory², and some further investigation of our model results shows these solutions are mathematically valid. By up-down symmetry, we may restrict our

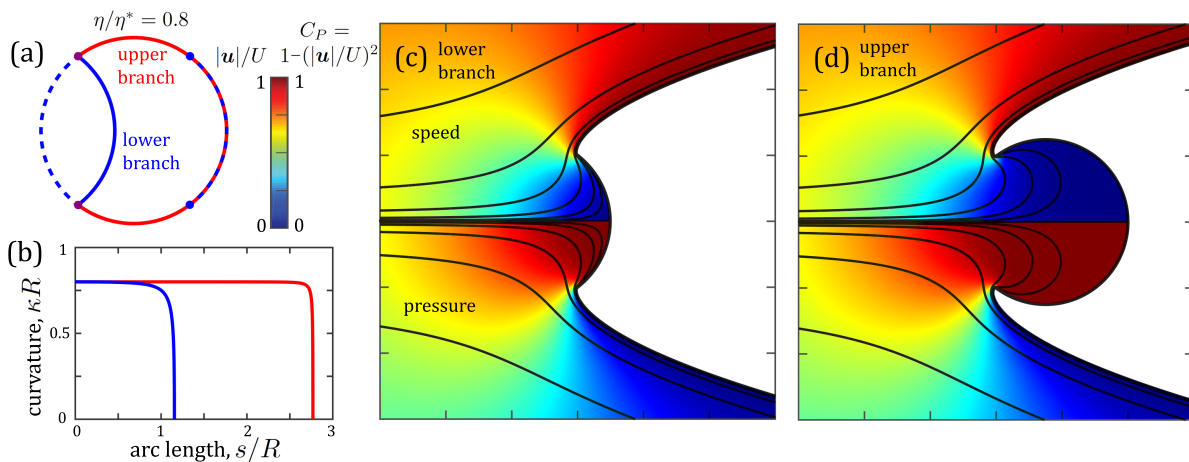


FIG. 5. Comparison of upper and lower branch solutions for $\eta/\eta^* = 0.8$. (a) The upper (red) and lower (blue) branch solutions are very nearly complementary arcs that complete a circle. The two dashed arcs are exact copies of the lower branch shape solution, reflected and translated downstream, respectively. (b) The two profiles show very nearly identical and uniform curvature for all but small regions near the pinning points. Speed and pressure maps for the (c) lower branch and (d) upper branch solutions.

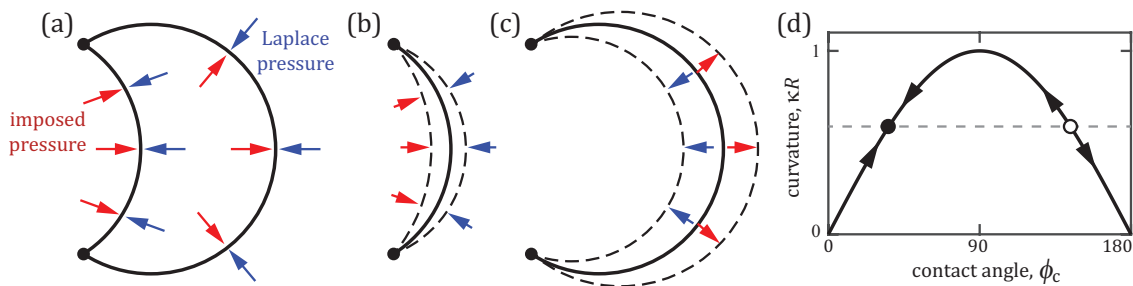


FIG. 6. Simplified interpretation of the equilibrium shapes and their stability. (a) Uniform and moderate external pressure (red) leads to two equilibria of the same curvature and thus same Laplace pressure (blue). (b) The sub-semicircular shape is stable. Inward deformations of the shape lower the Laplace pressure due to the drop in curvature, and the external pressure dominates and restores the shape. Outward deformations are restored due to increased Laplace pressure. (c) The super-semicircular shape is unstable by an analogous argument. (d) The slope of a curvature *vs.* contact angle plot explains the differing stability for sub- and super-semicircular arcs.

attention to the top half of the flow domain ($y > 0$). We note that the free streamline necessarily intersects the film in two locations, so there are two regions (\mathcal{R}_1 and \mathcal{R}_2) in the physical z -plane bounded by the free streamline and the film. The model predicts no fluid flow in the region \mathcal{R}_1 above the film; that is, $z(\zeta) \notin \mathcal{R}_1$ for ζ in the upper half-disk (Fig. 3c), where $z(\zeta)$ is defined in Eq. (13). On the other hand, the model predicts that $w(z)$ is double-valued in the region \mathcal{R}_2 below the film; that is, $z(\zeta_1) = z(\zeta_2) \in \mathcal{R}_2$ for distinct values ζ_1 and ζ_2 . The double-valued nature of $w(z)$ for $z \in \mathcal{R}_2$ arises from the overlapping of the solutions $w(z)$ above and below the film. The solution above the film satisfies the conditions $\text{Im}(w) = 0$ and $|dw/dz| = 1$ on the free streamline, but fails to satisfy the condition $\text{Im}(w) = 0$ on the film, while the solution below the film does the opposite. We drew these conclusions by numerically implementing the argument principle from complex analysis³; specifically, we used the trapezoidal rule to integrate the function $f'(\zeta)/f(\zeta)$ along the boundary of the upper half-disk of radius $R \lesssim 1$ in the ζ -plane, where $f(\zeta) = z(\zeta) - q$ and

q is an arbitrary point in the physical z -plane.

Returning to the comparison of the lower and upper branches (Fig. 5), we may interpret the two equilibria and their stability in the simplified setting of a film subject to an exactly uniform imposed pressure. (This situation may be realized by a film spanning one end of a tube whose internal hydrostatic pressure is greater than that outside.) As shown in Fig. 6(a), if the imposed pressure (red arrows) is moderate, there exist two shapes of the same curvature. By the Young-Laplace law, the surface tension pressures (blue arrows) are equal and thus both shapes satisfy the pressure balance needed for equilibrium. The less deformed solution would seem to be stable to shape perturbations, as shown in Fig. 6(b). Inward perturbations (less distended shapes) cause a decrease in curvature and a consequent drop in Laplace pressure, thus the imposed pressure dominates and restores the shape. Outward perturbations cause an increase in curvature and the consequent increased Laplace pressure restores the shape. The overly inflated solution, however, seems to be unstable, as argued in Fig. 6(c). Inward

perturbations increase curvature, which leads to further collapse of the film. Outward perturbations cause a drop in Laplace pressure and the dominance of the external pressure further inflates the film. This argument suggests the lower branch of Fig. 4 is stable and the upper is unstable.

This stability argument may be seen graphically in Fig. 6(d), where curvature is plotted for the family of circular arcs: $\kappa R = \sin(\phi_c)$. The key observation is that curvature, and thus Laplace pressure, displays a peak. On the left side of the peak, i.e. for sub-semicircular arcs, shape perturbations are restored by the Laplace pressure. To the right, i.e. for super-semicircular arcs, such perturbations lead to changes in Laplace pressure that further amplify the change in shape. Although the equilibrium profiles found in our model are not circular arcs, they are approximately so, suggesting that these conclusions

may still apply. Returning to the solution map of Fig. 4, it may then be concluded that, for a given $\eta/\eta^* < 1$, shapes converge towards the lower branch and repel away from the upper branch, as indicated by the arrows. For $\eta/\eta^* > 1$ no equilibrium solution exists, which may be associated with unbounded inflation of a film, and perhaps its subsequent rupture by thinning or the pinching off of a bubble. Unbounded inflation, rupture, or a bubble may also occur for $\eta/\eta^* < 1$, if the initial shape is sufficiently distended as to be above the upper branch.

¹S. Alben, M. Shelley, and J. Zhang, “How flexibility induces streamlining in a two-dimensional flow,” *Physics of Fluids* **16**, 1694–1713 (2004).

²A. R. Elcrat and L. N. Trefethen, “Classical free-streamline flow over a polygonal obstacle,” *Journal of Computational and Applied Mathematics* **14**, 251–265 (1986).

³J. W. Brown and R. V. Churchill, *Complex variables and applications* (McGraw-Hill, 2009).